Advances in Colloid and Interface Science 326 (2024) 103122

Contents lists available at ScienceDirect

Advances in Colloid and Interface Science

journal homepage: www.elsevier.com/locate/cis

Historical Perspective

In situ characterization of heterogeneous surface wetting in porous materials

Ying Da Wang [a], Luke M. Kearney [b], Martin J. Blunt [d], Chenhao Sun [c], Kunning Tang [a], Peyman Mostaghimi [e], Ryan T. Armstrong [e,*]

[a] School of Minerals and Energy Resources Engineering, University of New South Wales, Sydney, NSW 2052, Australia
[b] Department of Earth Sciences, University of Oxford, Oxford OX1 3AN, United Kingdom
[c] State Key Laboratory of Petroleum Resources and Prospecting & College of Geosciences, China University of Petroleum, Beijing 102249, China
[d] Department of Earth Science and Engineering, Imperial College London, London SW7 2AZ, United Kingdom
[e] School of Civil and Environmental Engineering, University of New South Wales, Sydney, NSW 2052, Australia

ARTICLE INFO

Keywords:
Contact angle
In situ wettability
Topology
Porous media
Multiphase flow

ABSTRACT

The performance of nano- and micro-porous materials in capturing and releasing fluids, such as during CO_2 geo-storage and water/gas removal in fuel cells and electrolyzers, is determined by their wettability in contact with the solid. However, accurately characterizing wettability is challenging due to spatial variations in dynamic forces, chemical heterogeneity, and surface roughness. *In situ* measurements can potentially measure wettability locally as a contact angle - the angle a denser phase (e.g water) contacts solid in the presence of a second phase (*e.g.* hydrogen, air, CO_2) - but suffer from difficulties in accurately capturing curvatures, contact areas, and contact loops of multiphase fluids. We introduce a novel extended topological method for *in situ* contact angle measurement and provide a comparative review of current geometric and topological methods, assessing their accuracy on ideal surfaces, porous rocks containing CO_2, and water in gas diffusion layers. The new method demonstrates higher accuracy and reliability of *in situ* measurements for uniformly wetting systems compared to previous topological approaches, while geometric measurements perform best for mixed-wetting domains. This study further provides a comprehensive open-source platform for *in situ* characterization of wettability in porous materials with implications for gas geo-storage, fuel cells and electrolyzers, filtration, and catalysis.

1. Introduction

Wettability defines the relative affinity for one fluid to coat the surface of a given solid over another fluid. This relative adhesion of two fluids to a solid occurs widely in natural and industrial processes involving multiphase flows in porous media, such as CO_2 sequestration [1,2], H_2 gas production and storage [3,4] in porous rocks, and gas and water flows in hydrogen electrolysers and fuel cells [5–7]. In these systems, the wettability distribution across the solid surface is known to vary and has a profound effect on pore-scale flow patterns, which greatly influence large-scale factors such as injectivity, productivity, and recovery in geological storage and production, and overall energy density and efficiency of hydrogen-based electrochemical cells [8].

Contact angle measurement is a widely used method for characterizing the wetting properties of a solid surface and is defined as the angle formed between the solid-liquid-vapor (or solid-liquid-liquid in the case of two immiscible liquids) triple line at the point of contact between a liquid drop and a solid surface, measured through the denser (usually aqueous) phase. There are several methods available for measuring the wettability of a two-fluid and solid material, including *ex situ* measurements involving the use of averaged estimates at the cm-scale such as the Amott and USBM indices [9], laboratory measurements on smooth pure mineral surfaces, and underlying numerical methods involving molecular dynamics [10] or modeling disjoining pressures [11]. These methods make the assumption of smooth surfaces and an absence of mineralogical or chemical heterogeneity within the pore space of real materials due to either averaging above the scale of the contact line in *ex situ* methods, or a limited spatial domain in molecular dynamics simulations. In addition, in 3D space the common contact of three phases forms a contact loop with its own complex geometry rather than the commonly used (and misleading) terminology of a common line.

* Corresponding author.
E-mail address: ryan.armstrong@unsw.edu.au (R.T. Armstrong).

https://doi.org/10.1016/j.cis.2024.103122
Received in revised form 28 February 2024;
Available online 11 March 2024
0001-8686/© 2024 The Authors. Published by Elsevier B.V. This is an open access article under the CC BY license (http://creativecommons.org/licenses/by/4.0/).

In recent years, there has been increasing interest in developing techniques for *in situ* measurement of contact angle, which allows for the real-time determination of the wetting properties of a surface under operating conditions, mapped directly to the pore structure. This is particularly important in situations where the contact angle may change due to external factors such as temperature, humidity, applied pressure [12,13], or ongoing surface reactions [14,15]. By leveraging micro-scale imaging of porous media using X-ray micro computed tomography (micro-CT), multiphase fluid configurations are directly visible and measurable. Initial manual measurements on three-phase contact loops [16] have been successfully used for characterization [17], but their limited data throughput and inherent measurement biases have given way to automatic methods on segmented micro-CT images. These automatic *in situ* methods can have evolved from measurements using a segmented voxelized image of the fluids and solids [18], which struggles with aliasing (though deep learning has alleviated this somewhat [19,20]), to measurements on smoothed meshes of fluid clusters [21], which are reliant on accurate three-phase contact loop identification and smooth meshing algorithms that minimize deformation. A different methodology has also been proposed and implemented on pore-scale multiphase images involving the integration of surface curvatures of fluid bodies using principles of topology to determine the wettability [22–25], which have been shown to be less sensitive to changes in voxel resolution and accuracy of the three-phase contact loops as the method in its original form does not require identification of the solid-fluid interface and incorporation of the surface and contact loop orientations. With these considerations, it remains unclear which of these methods is most suitable, and the overall availability of implementation of these *in situ* methods remains low due to the complexity of the methodology. In the public domain, aside from this study and its associated implementation, there exists no available repository of topological methods [22–25], while geometric implementations exist [18,19,21].

In this paper, a detailed description and associated software package of the most recent and widely used computational methods are presented for *in situ* measurements of wettability in multiphase porous media. This includes (a) direct measurement of the geometry of smoothed meshes of fluid clusters; (b) integration of surface curvatures of fluid bodies using principles of topology; and (c) a new, more generalized formulation of the topological method – an extended topological method. This formulation accounts for deviations associated with solid surface orientation, and the meshing algorithm retains sensitivity to three-phase contact loop identification and mesh quality. The relative accuracy, limitations, and advantages of these methods are explored on ideal cases of droplets on smooth and curved surfaces, as well as their relative accuracy in probing the wettability within porous media. A full analysis of meshing sensitivity in relation to measured wettability is performed, as this pre-processing step is a key limitation of these methods. It is found that the extended topological method performs similarly to direct geometric measurements on meshes for uniformly wetting porous systems, while the original topological method deviates in accuracy at intermediate wettabilities. For mixed-wet systems, geometric methods continue to outperform topological methods due to increased sensitivity to surface curvature for complex cluster geometries, especially in mixed-wet systems where the local contact angle is an important value to estimate, aside from the overall wetting characteristics of a domain. Since many materials involve the interplay between complex geometries and variable wetting sub-materials, the use of *in situ* measures of wettability in the characterization and design of advanced porous materials for fluid and energy transfer has the potential to significantly enhance their performance and efficiency in a variety of applications.

2. Materials and data

This study uses a series of increasingly complex meshed domains to (i) validate the inherent accuracy of each contact angle measurement method, (ii) their robustness when applied to voxelized simple geometries, and (iii) application to complex real porous media from simulations and segmented micro-CT images. These meshed domains are depicted in Fig. 1.

2.1. Perfectly meshed sphere on a flat or curved surface

To investigate the inherent accuracy in measuring the contact angle of a fluid body in contact with a solid surface surrounded by another fluid, a near-perfect spherical mesh is generated on a flat meshed surface by the Young-Laplace equation. The intersection of the spherical mesh and flat surface form the fluid-solid interface, which retains a sharp geometry (see Fig. 1), and is shifted along the diameter of the sphere to model contact angles from 2^o to 178^o.

2.2. Voxelized sphere on a flat or curved surface

Since micro-CT images (and 3D pore-scale images from other imaging sources) are voxelized at varying levels of detail, a surface and sphere are generated by the segmentation of a Euclidean Distance Transform in a cubic voxel domain at different resolutions. The solid surface in these cases is also modeled by either a flat voxel surface, or a spherical grain, on which the spherical phase body sits. These voxelized cases represent the type of geometric detail and voxel-aliasing found in real micro-CT images of multiphase fluid configurations in porous

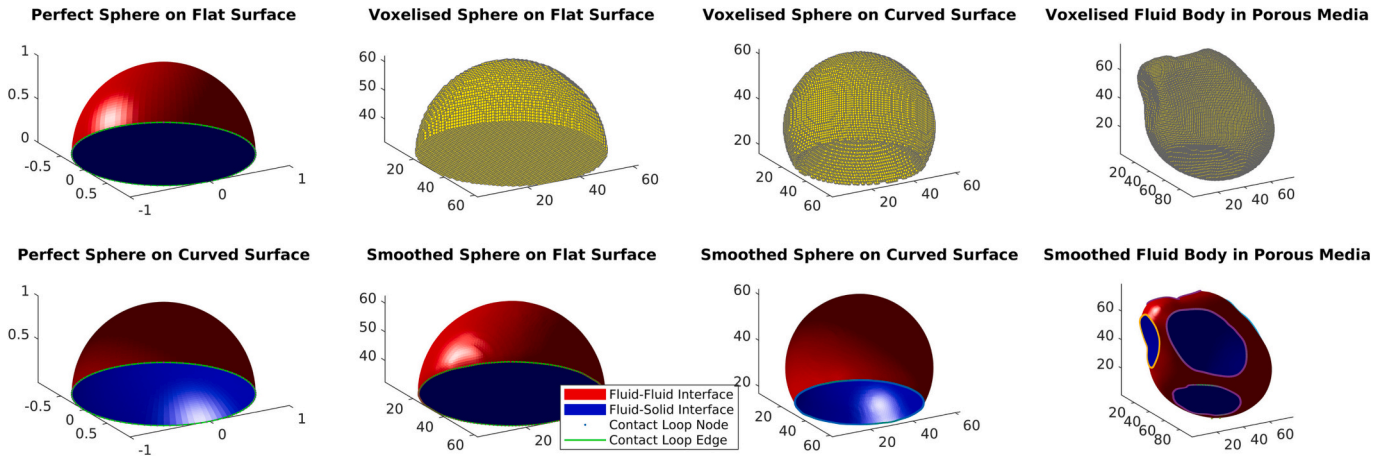


Fig. 1. Examples of the various fluid configurations tested in this study. Perfect meshes test inherent mathematical accuracy, smoothed meshes from voxelized volumes test sensitivity to geometrical errors, and curved/real fluid bodies test overall accuracy.

media. The level of detail in these domains represents both the intrinsic size of a phase body, as well as the imaging resolution available. Example configurations are shown in Fig. 1.

It is important to mention that, due to voxel aliasing, as a sphere (or any geometry) is characterized by fewer and fewer voxels, the intrinsic intended geometry of the object deviates from the generated (or imaged) object. For example, the extreme case of a sphere described by a $2 \times 2 \times 2$ voxel domain becomes a cube. The issue of recovering the intrinsic geometry of such a highly aliased object is ill-posed, and this study addresses this issue with a convergent meshing approach outlined in Section 3.1.2.

2.3. Voxelized multiphase fluid configurations in porous media: CO_2/H_2 geo-storage and a proton exchange membrane fuel cell

In voxelized images of multiphase fluid configurations in porous media, there exist further considerations of image quality [26,27], multi-label segmentation accuracy [28,29], and complex solid-fluid geometries beyond the simple Young-Laplace droplet mentioned previously. These factors significantly increase the uncertainty of what the intrinsic geometry of a voxelized fluid body should be. Image noise and segmentation errors are key factors that cause high sensitivity in measuring contact angles, and is especially the case for aliasing of small fluid bodies and complex solid geometries. As such, this study also uses images obtained from multiphase fluid flow LBM simulations [30–32] on micro-CT images of (i) CO_2 gas storage in water saturated Bentheimer sandstone rock, and (ii) liquid water transport in an air-saturated gas diffusion layer (GDL) of a Proton Exchange Membrane Fuel Cell (PEMFC) [6]. The sandstone domain measures 1000^3 voxels at a resolution of 5.3 μm/voxel and represents a typical target domain for CO_2 or H_2 geostorage, whereas the GDL of the PEMFC measures $2000 \times 2000 \times 400$ voxels at a resolution of 700 nm/voxel, representing a typical porous structure present in the layers of a fuel cell or electrolyzer for optimisation of the cross-flow and cross-diffusion of gas and water.

3. Methods

3.1. Preparation of the geometry

3.1.1. Meshing isolated voxelized fluid clusters

From a multiphase segmented micro-CT image of, for instance, solid (s), water (w), and gas (g), the water phase is considered phase 1 (the denser phase), while the gas is phase 2. Individual clusters of the phase of interest are isolated by connected components analysis. This phase of interest is typically the phase with a lower overall saturation and/or the phase that is predominantly non-wetting as these conditions result in a larger number of isolated fluid clusters for analysis. In this paper, for simple examples, we will isolate clusters of phase 1 by default; later when mixed-wet media are analyzed clusters of both phases will be considered. From here, the fluid-fluid interface and the fluid-solid interface of each isolated fluid cluster is identified. As there are 3 phases present – solid (s), and phases 1 and 2, two binary boundaries can be extracted; *(i)* between the solid and the two fluids Γ_{s-12} and *(ii)* the boundary between the isolated phase and the surrounding phase and solid Γ_{1-s2}. These boundaries are meshed by performing the marching cubes algorithm [33]. From these meshes, as they were triangulated on the exact voxel geometry, their intersection forms the fluid-solid boundary mesh as $\Gamma_s = \Gamma_{1-s2} \cap \Gamma_{s-12}$, while the fluid-fluid boundary is the subtraction of the fluid-solid boundary from the cluster surface as $\Gamma_f = \Gamma_{1-s2} \setminus \Gamma_s$. From these meshed interfaces, the contact loops S_{fs} can be extracted by identifying which of the edge elements of all triangles in Γ_f are unbounded (edges that only exist within 1 triangle). This edge identification operation applies to all triangles on the surface mesh as a list of all edges of all triangles, and edges that only occur once are the edges of the entire surface. The loops formed from these unbounded edges form the contact loops. This process is visualized in Fig. 2.

3.1.2. Smoothing meshed fluid clusters

After cluster isolation and surface/contact loop identification as described in the previous section, the meshes need to be smoothed to measure contact angles within reasonable precision. As the surfaces and the contact loops have been identified, they are smoothed separately to maintain sharpness along the three-phase contact loop. Mesh smoothing

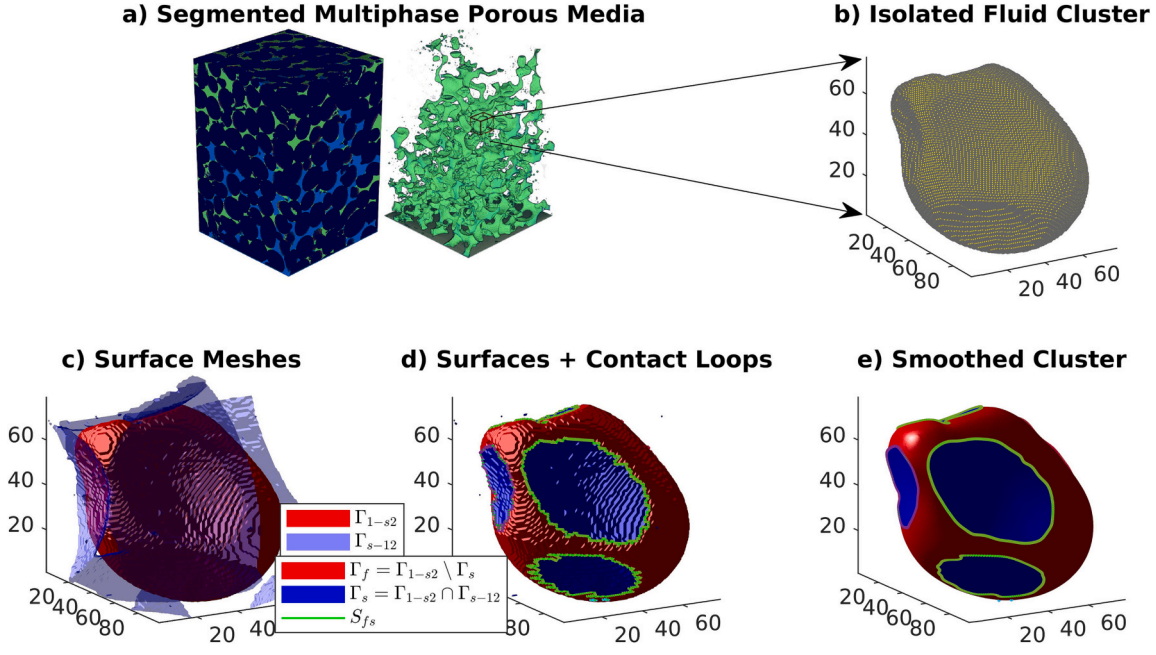


Fig. 2. Depiction of the workflow for cluster isolation, surface identification, and mesh smoothing.

falls under two main categories; shrinking and volume preserving, with each method possessing benefits and drawbacks.

In this study, the shrinking method performs neighborhood coordinate averaging for each node on a mesh (Laplacian smoothing [34]), that is, the coordinates $\vec{X}_N$ of node N are updated to be the mean value of the neighboring nodes connected by edge elements N_e such that $\vec{X}_{N_{smoothed}} = \frac{\sum_e N_e}{\sum_e e}$. This smoothing requires relatively few iterations to achieve a smooth surface, but will cause shrinkage in convex regions and expansion in concave regions. A volume-preserving smoothing is also applied in this study which reduces volume shrinkage but requires many iterations to smooth a surface. The algorithm developed for this study involves first performing standard shrinking smoothing, then computing the normal vectors of the shrunken smoothed surface, projecting the shrunken coordinates back along these normal vectors the same distance that they were displaced during the shrinking step. This is repeated over many iterations to result in a stable smoothing that preserves the original volume of the cluster. The projection distance is scalable to allow small degrees of volume shrinking and expansion per iteration. Neither method is capable of adequately smoothing a fluid cluster without a degree of volume shrinkage and thus, a volume shrinkage threshold of 5% of the original cluster volume is used in this study (see Section 4.2).

3.2. Contact angle measurement

3.2.1. Geometric contact angle calculation

As the methodology for fluid cluster meshing in this study explicitly isolates the contact loops and employs separate smoothing routines for lines and surfaces [21] (see previous Section 3.1.1), the contact angle along the nodes of the contact loop (Fig. 3a) can be measured directly on the geometry of the cluster. The normal plane N_{plane} to the contact loop can be defined using the node coordinate of $\vec{X}_N$ and normal vector $\vec{N}$ approximated by the secant drawn by the neighboring contact loop nodes $\left[\vec{X}_{N-1}, \vec{X}_{N+1}\right]$ of each contact loop node (Fig. 3b). This normal plane is then intersected with the cluster mesh Γ_{1-s2}, and the angle made by the nearest nodes in the intersected polygon are used to measure the contact angle directly (Fig. 3c). This measurement directly on the mesh achieves a similar outcome to measuring the dot product of the normal vectors of the fluid and solid mesh surfaces [21].

3.2.2. Topological contact angle calculation

A topological approach to contact angle measurement that minimizes the uncertainty of segmentation and identification of the contact loop can be developed with fundamental concepts from integral geometry [23,24] and the deficit curvature [22]. This term, referred to as θ^{macro}, is not strictly a measure of the contact angle, rather it is a measure of the wetting state of a system [35]. This is defined as an approximate relationship between the topology (*i.e.*, curvature) of the fluid body and the contact loop as:

$$\theta^{macro} = \frac{4\pi\chi - \sum \kappa_{G_i} A_i}{4N_{loops}}, \tag{1}$$

where χ is the Euler number, κ_{Gi} is the Gaussian curvature of triangular element i of any given surface element of the fluid body, and A_i is the element area, and N_{loops} is the number of contact loops. This calculation of the topological contact angle, also referred to as the macroscopic contact angle, is a relatively straightforward calculation as it only requires the computation of the Gaussian curvature (the product of the two principal curvatures) over a smoothed mesh of the entire fluid body $\sum \kappa_{G_i} A_i$, the Euler number χ, and the number of contact loops N_{loops}. This results in the calculation being less sensitive to the curvatures near the microscopic contact point, and independent of any need to measure sharp angles along the contact loops and interfaces. Due to the inherent simplifying assumptions in this calculation, θ^{macro} does not directly map to a geometric contact angle for geometric angles near 45^o and 135^o, which exhibit under and over estimation, respectively [35]. Fig. 4a-c depicts the required steps involved per cluster to compute the terms within the topological calculation method.

The Euler number or the Euler-Poincare characteristic of the isolated cluster is a topological invariant used in image analysis to characterize the connectivity of structures within an image, and is calculated as $\chi = V - E + F$, where χ is the Euler number, V is the number of vertices, E is the number of edges, and F is the number of faces [36]. The Gaussian curvature κ_i of a given element i is calculated on each node by calculating the local least-square quadratic surface fit, then the eigenvectors and eigenvalues of the Hessian are used to calculate the principal, mean and Gaussian curvatures. The per-element values are then given by the mean of the nodal values per triangular element. Due to the ill-posed nature of mesh smoothing of voxelized domains (see Section 3.1.2), the curvatures of even smoothed surfaces are rather noisy due to imperfections on the mesh surface. These issues are alleviated by the weighted area averaging effect of the $\sum \kappa_{G_i} A_i$ term, which returns a scalar average curvature of the cluster surface.

3.2.3. Extended topological contact angle calculation

The relationship between the Gauss-Bonnet Theorem and wettability can be generalized to an expression for the deficit curvature for the meniscus of a cluster with an added term ϕ that accounts for the orientation of the solid surface. This eliminates the discrepancy between the topological contact angle introduced in the previous section (which does not consider ϕ) and geometric contact angle calculations at

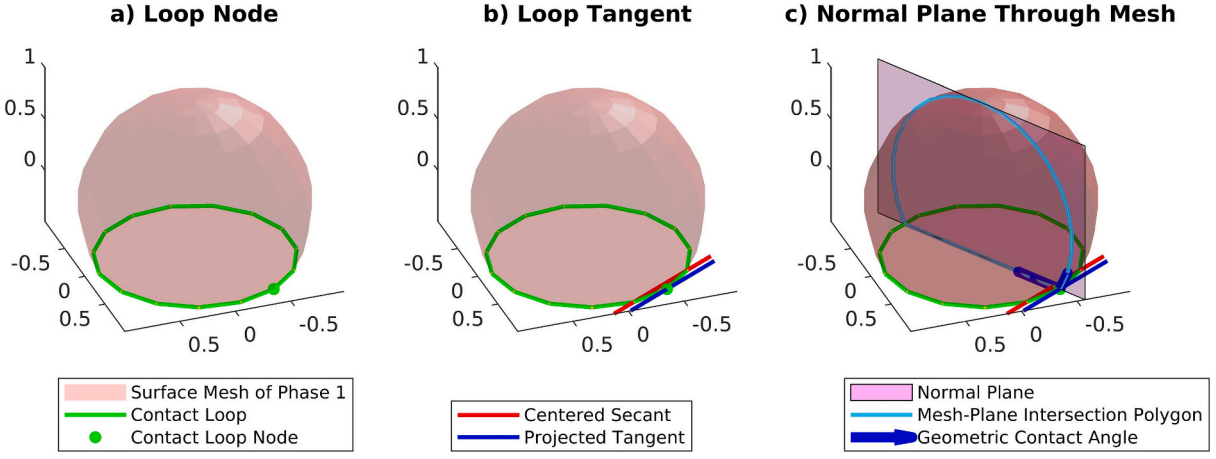


Fig. 3. Geometric contact angle measurement on the smoothed mesh.

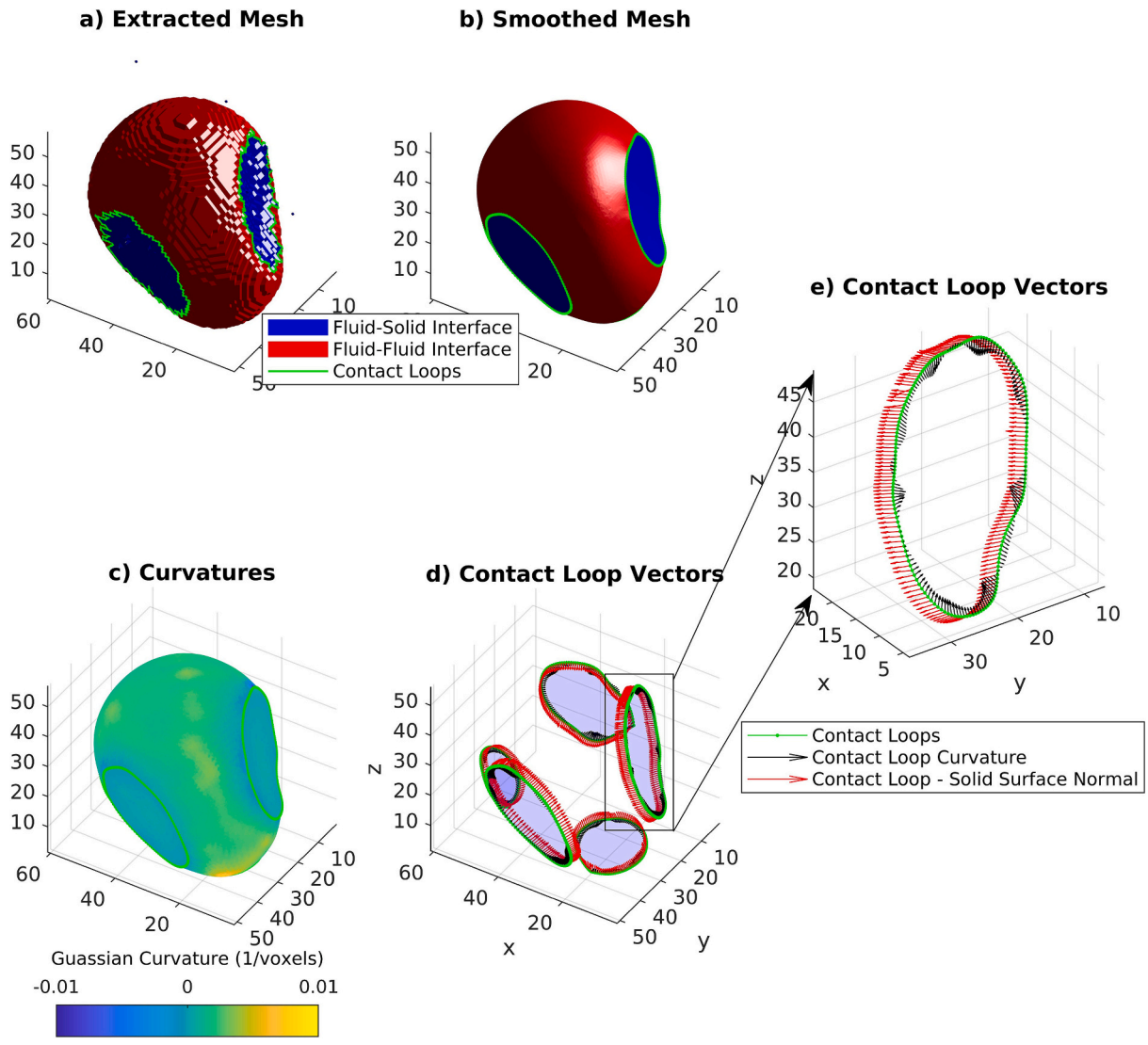


Fig. 4. Depiction of processing steps to calculate the topological, Eq. (1) and extended topological contact angle, Eq. (2). With the curvature of the surfaces (a-c), the topological contact angle outlined in Section 3.2.2 can be calculated. With additional steps to identify contact loops, their curvatures and surface normals (a-e), the extended topological contact angle in Section 3.2.3 can be calculated.

intermediate acute and obtuse angles. A full derivation can be found in the Appendix.

$$\phi = cos^{-1}\left(\vec{\kappa}_{line} \bullet \vec{N}_s\right)$$

$$\theta_{extended} = \phi - \frac{\pi}{2} + cos^{-1}\left(1 - \frac{4\pi n_f - \sum \kappa_{G_{if}} A_{if}}{2\pi N_{loops}}\right), \quad (2)$$

where $\vec{\kappa}_{line}$ is the curvature of the contact loop nodes, $\vec{N}_s$ is the normal unit vector to the solid surface at the contact loop nodes, κ_{Gif} is the Gaussian curvature of element i_f on the fluid-fluid interface, A_{if} is the element area, and n_f is the number of separate fluid-fluid interfaces which is calculated by iteratively indexing the connectivity of elements on the fluid-fluid interface mesh surface. Separate fluid-fluid interfaces will contain a closed list of connected nodes and elements. This calculation is more geometrically complex compared to the simpler calculation in Eq. (1), and requires accurately identified and smoothed contact loops. Alongside the previously mentioned separate meshing of the fluid-fluid (Γ_f) and the fluid-solid (Γ_f) interfaces and the contact loops (S_{fs}) in Section 3.1.1, as well as the calculation of the Gaussian curvature κ_i, further calculations of contact loop curvature and solid-fluid interface normal at the contact loop ($\vec{\kappa}_{line} \bullet \vec{N}_s$ in Eq. (2)) are then required to evaluate Eq. (2). Fig. 4a-e depicts the required steps involved per cluster to compute the terms within the topological calculation method.

4. Results and discussion

4.1. Comparison for perfectly smooth meshes on flat and curved surfaces

To clarify the intrinsic precision of each contact angle measurement technique, an initial comparison is conducted on spherical meshes created by employing distance functions. This approach enables the production of almost flawless spherical meshes, which are subsequently altered by incorporating either a planar solid-fluid boundary or a progressively curved one. The intersection between the spherical mesh and the flat surface creates the solid-fluid boundary, maintaining a well-defined geometry. This intersection is moved along the sphere's diameter to simulate contact angles ranging from 2^o to 178^o.

The resulting contact angles measured and depictions of the meshes used are shown in Fig. 5. A clear match is seen with geometric measurement and the extended topological method (Eq. (2)), while significant deviation occurs with the original topological method (Eq. (1)) at

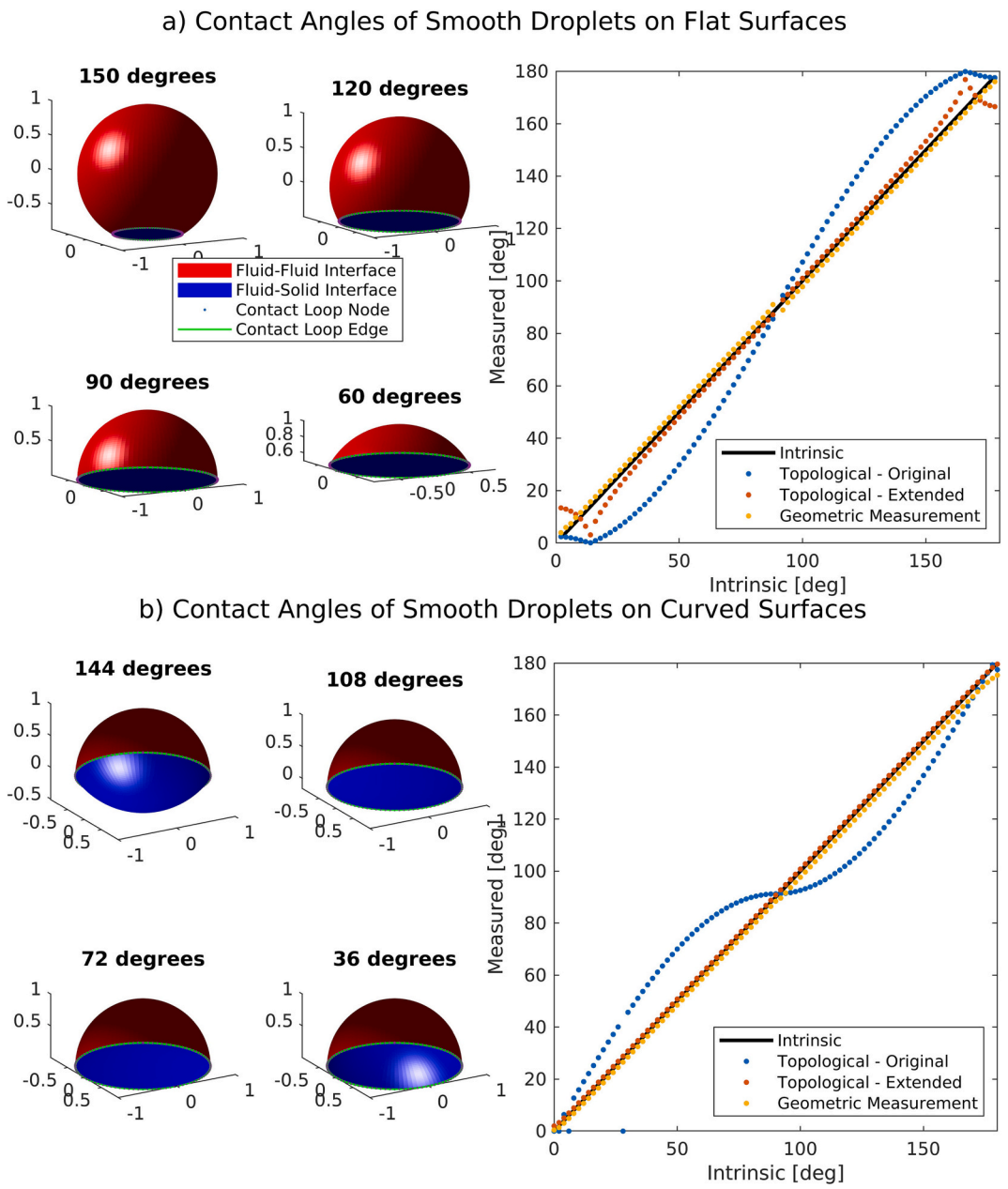


Fig. 5. Comparison of the inherent accuracy of contact angle measurement for each method. We assume that phase 1 is contained within the droplets shown. (a) Shows the case of a spherical droplet on a flat surface, while (b) shows the case of a hemispherical droplet on a curved surface. Both examples exhibit clear deviations in the original topological measurement method (Eq. (1)), whereas the extended topological calculation (Eq. (2)) and the geometric measurement methods closely match the intrinsic value.

acute and obtuse angles, peaking at 45^o and 135^o. This discrepancy is due to the mapping of the topological contact angle (which is a measure of the wetting state rather than explicitly the contact angle) to the geometric contact angle as was discussed in [23]. The deviation of the extended topological contact angle measurement at extreme angles is due to numerical approximation errors in calculating the Gaussian curvature of the spherical mesh at extremely flat angles. The method of calculating the local curvatures outlined in Section 3.2.2 results in approximation errors due to attempting to fit a paraboloid on increasingly flat surfaces at extreme angles.

4.2. Comparison on voxelized meshes

On meshes of fluid clusters that originate from voxelized images (such as segmented micro-CT data), there are extra sources of uncertainty in the calculation of contact angle. The main issues are (i) the ill-posed smoothing of the mesh that causes divergent deformation, and (ii) the aliasing that occurs on fluid clusters that are characterized by few voxels. In both cases the value of the intrinsic contact angle of a fluid cluster becomes unknown. This problem is exemplified in Figs. 6 and 7, which show the measured contact angles as they change with continued mesh deformation and low-resolution aliasing. The case in Fig. 6 shows a hemispherical fluid cluster on a flat surface, with an intrinsic contact angle of 90^o. This is generated using distance functions on voxelized domains. It becomes visually evident that for a spherical diameter (D) of approximately below 16 voxels (and clear in the case of $D = 8$ voxels) that the relationship between the voxel geometry of the cluster and the intrinsic contact angle is non-existent. This aliasing is also evident in the case of the fluid clusters on curved solid surfaces in Fig. 7.

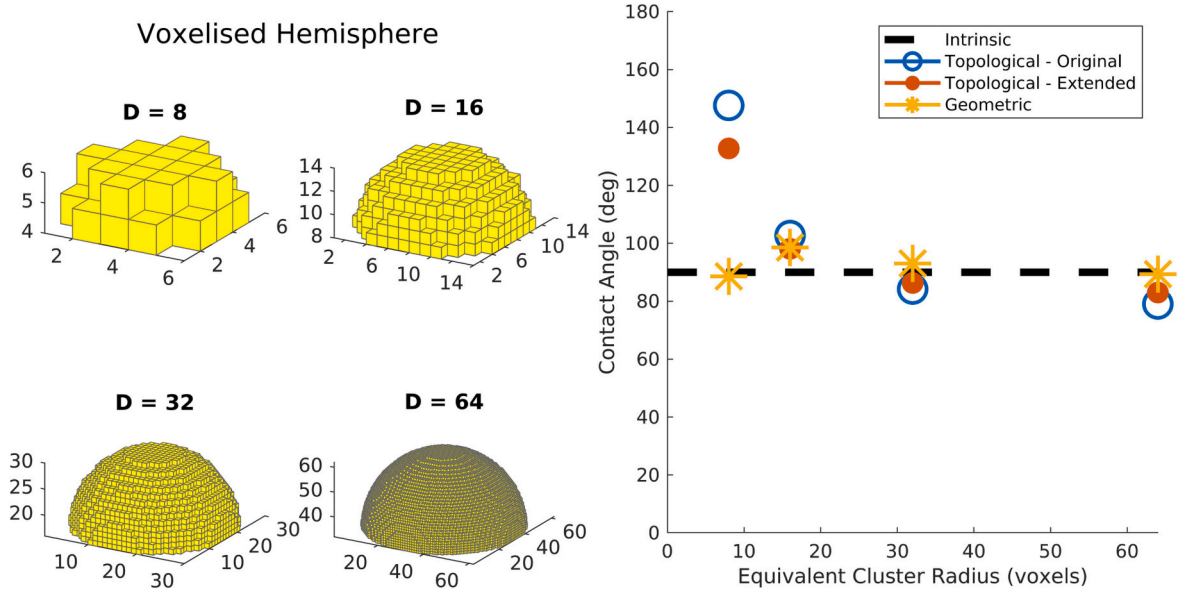


Fig. 6. Left: Visual render of voxelized fluid clusters of hemispheres at diameters of 8, 16, 32, and 64 voxels. Right: Calculated contact angle of these fluid clusters as a function of the calculation method and the equivalent cluster radius. The concept of an intrinsic contact angle breaks down around D < 16 due to aliasing, and smoothing results in a reasonable calculated value of the contact angle at 5% shrinkage for D > 8 for geometric and D > 16 for topological methods. The geometric method performs most consistently as it does not require surface curvatures, and the smoothing algorithm in this study preserves contact loop sharpness which is flat in the z-direction.

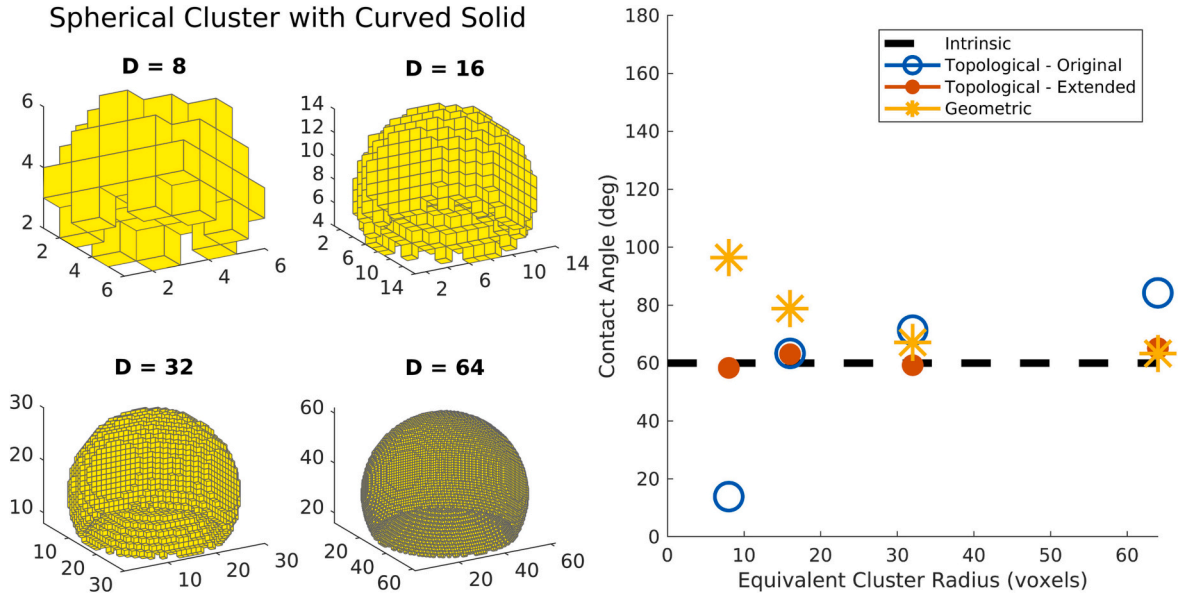


Fig. 7. Left: Visual render of voxelized fluid clusters of spheres on curved surfaces at diameters of 8, 16, 32, and 64 voxels. Right: Calculated contact angle of these fluid clusters as a function of the calculation method and the equivalent cluster radius. In this case, the geometric method and the extended topological methods perform most accurately since the smoothing of surfaces plays a larger role and the contact loop is affected by aliasing in 3 orientations. The original topological method shows its characteristic acute/obtuse angle deviation.

The resulting measurements of contact angle for these clusters (D = 8,16,32,64 voxels) using each of the contact angle measurement methods (Geometric, Topological, Extended Topological) are shown for a volume shrinkage factor of 0.95 (5% shrinkage). The volume shrinkage factor is defined as $\left(F_{shrinkage} = 1 - \frac{V_{current}}{V_{initial}}\right)$ and can be used to gauge the extent that mesh smoothing remains within the bounds of the intrinsic contact angle. Plots of the full shrinkage range can be found in Supplementary Materials Fig. 1 in the Appendix, showing 5% to 15% shrinkage as the sweet spot for cluster accuracy. From the plots in Figs. 6 and 7, it can be seen that mesh smoothing can be considered valid for spherical clusters at 5% volume shrinkage based on rapid convergence of the geometric method and the extended topological methods.

A slightly slower convergence of topological methods to the intrinsic value can be seen for the hemispherical case (surface curvature error dominates), while the geometric method converges slower for the curved surface case (contact loop error dominates). These errors can be qualitatively defined as the deviation of the measured values relative to the case of a perfectly meshed equivalent object, such as those generated in Section 4.1. Since geometric methods do not use any surface curvature information while the original topological method exclusively uses

surface curvature and the extended topological method uses a combination of surface curvatures and contact loop vectors, the hemispherical voxelized fluid clusters intrinsically have less deviation in their contact loop error due to the 2D flat-bottom geometry of the fluid-solid interface. This means that any differences between the accuracy of topological and geometric methods for the case of a hemispherical cluster is naturally dominated by the surface curvature error. In the case of curved fluid-solid surfaces, the contact loop formed by the smoothing of the voxelized geometry is much more sensitive to aliasing due to the surface varying in 3D and as such, the observation that geometric methods converge slower is due exclusively to these contact loop errors as geometric methods are not dependent on surface curvature.

The geometric and extended topological methods perform well from $D \in [8,64]$, but in general, all methods require a higher quality mesh from $D \in [16,64]$ for a reliable result. The characteristic deviation at acute angles when calculating contact angles with the topological method is also apparent in Fig. 7, as the topological method overestimates the contact angle compared to the geometric and extended topological measurements. Overall, the geometric method and the extended topological methods perform most consistently over the mesh smoothing and voxel aliasing range though topological methods require higher levels of mesh detail due to surface curvature calculations being more sensitive to voxel aliasing. The high accuracy of the geometric method is due to the algorithm outlined in Section 3.1.1 that discretely isolates contact loops and Section 3.1.2 that performs smoothing operations separately on surfaces and lines, which preserves the accuracy and sharpness of the angles formed at the contact loops by the fluid-fluid and fluid-solid interfaces. While the contact loop geometry is critical for the extended topological method, topological methods are also extremely sensitive to the $\sum \kappa_{G_i} A_i$ term – the sum total cluster Gaussian curvature.

4.3. Comparison on variably wetted micro-CT images of porous structures

With the validation of the contact angle methods on perfect meshes as well as analysis of their accuracy and sensitivity on voxelized meshes, the performance of these methods can be analyzed on real images of porous structures. A shrinkage factor of 5% is chosen for these cases based on the convergence results shown in the previous section, which indicate <10% error in cases with $D > 8$ voxels for geometric methods and < 20% error in cases with $D > 16$ voxels for topological methods. The porous structures and fluids used in this case are (i) hydrogen/CO_2 gas storage in sandstone rocks, and (ii) liquid water and gas flow through the Gas Diffusion Layer (GDL) of a Proton Exchange Membrane Fuel Cell (PEMFC). In these simulations, the wettability on the surface of the rock and GDL are uniformly varied, with the sandstone case assumed to be water wetting and the GDL case assumed to be gas wetting (hydrophobic). The contact angles, measured through the water, tested for these cases are 60^o, 30^o, 0^o for the sandstone and 120^o, 150^o, 180^o for the GDL. The simulations are performed using Lattice Boltzmann Methods [31,32] whereby the contact angle is assigned as a surface affinity value, and the non-wetting phase saturation (gas for the sandstone and water for the GDL) is set at 30% for the sandstone and the GDL to emulate near-residual saturation cases, as well as maximize cluster isolation to improve the accuracy of the contact angle measurement methods. The initial condition of these domains is set with no external forces, and the initial fluid distribution is set to a saturation of 30% water for the GDL and 30% gas for the rock sample. This saturation is set in the initial condition of the domain by randomly flipping 30% of pore voxels to the desired phase. This uniformly random distribution is an approximation at these millimetre length scales for a condensation process. The result of this spinodal decomposition approach is that the LBM simulation will coalesce the clusters naturally as the simulation progresses. A small periodic boundary condition pressure gradient is imposed at the inlet-outlet boundaries (z-axis in this case) to drive the interfaces under a capillary dominated flow regime. Once the simulation reaches a steady state (approximated by running for 10,000,000 timesteps [30]), the boundary condition driving forces are set to zero for 1000,000 further timesteps. These fluid distributions are rendered in Fig. 8, and the computed contact angles of the clusters within each multiphase domain are shown in Fig. 9.

From the measurement contact angle distributions in Fig. 9, the relative accuracy of each measurement method can be compared. For intermediate contact angles (30-60^o and 120-150^o), it is clear that geometric measurements and the extended topological method perform similarly accurately, while the original topological method deviates as expected, under-estimating the wettability by 10-30^o. On the other hand, for highly wetting or non-wetting cases (0 and 180^o), the most accurate measurements are from the original topological method. This is likely partially due to the method not requiring measurements of the contact loop vectors, which as can be seen in previous Section 4.1 can be distorted at extreme angles for the extended topological and geometric methods when the cluster contacts with the solid surfaces are highly spherical with small contact areas, and only requiring surface curvatures that are increasingly accurate when clusters are more spherical. The geometric measurement tends to also produce values with a wider variance on a per-cluster basis due to mesh and geometry variation. The topological measurements of contact angle effectively produce a single number (original method), or a very tight band of values (extended method) per fluid cluster, which represents the “macroscopic contact angle” of the cluster. This results in a tighter distribution of measurements on a well-meshed domain. However, this can also result in increased outliers at intermediate wettabilities, as clusters in these cases are less sensitive to the fluid interface curvature while also possessing more varied contact loop geometries. Overall, the geometric method and the extended topological method produce similar accuracy in the case of measuring the overall wettability of a porous system.

Observing the global variation *versus* the cluster size of the calculated contact angle per cluster in Fig. 10 shows that the direct geometric measurement method provides a more reliable and less noisy measurement on a per-cluster basis. Topological and extended topological methods show higher deviation in the measured contact angle at equivalent cluster radii below 20 voxels. This is consistent with observations from previous sections on spherical clusters and is due to the increased sensitivity of the surface curvature to voxel detail and aliasing. For the measurement of the mean wetting characteristics however, these small clusters do not represent a significant number of measurements over their contact loop perimeters and thus do not show a strong effect in the histograms in Fig. 9. For the sandstone image, small clusters below 12 voxels equivalent radius constitute 10% of the total datapoints within the histograms. These deviations at smaller cluster sizes pose a significant problem for topological methods to map out the internal wettability distribution of a mixed-wetting domain, as each cluster becomes an important spatial data point. This is explored next in Section 4.4.

4.4. Spatial measurement and in situ wettability calculation for a mixed wetting gas diffusion layer

Validating and comparing the accuracy of the extended topological method, the original topological method, and the geometric measurement methods of contact angles on ideal fluid clusters as well as on fluid clusters within uniformly wetting porous structures in the previous sections only tests the ability of the methods to capture an average contact angle. *In situ* contact angle methods also need to accurately characterize the distribution of wettability. Many systems are mixed-wet with both hydrophilic and hydrophobic regions of the pore space. In these cases, the accuracy of the local contact angle measurement becomes the prevailing metric rather than an average measure of the system.

To benchmark the accuracy of recovering the local mixed-wetting contact angle distribution, the gas diffusion layer domain used thus far in this study is assigned a Gaussian distribution of local contact angle

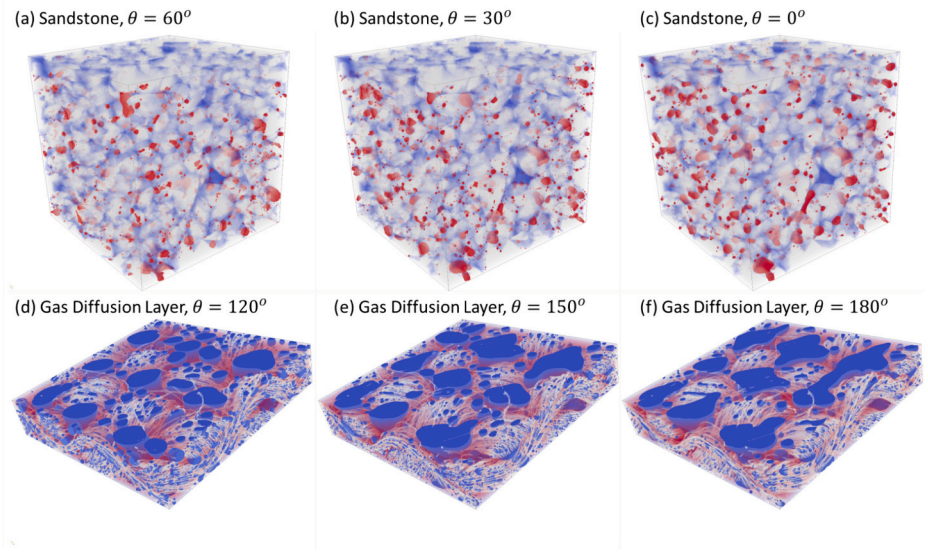


Fig. 8. Visual renders of the fluid distributions within the porous structures of sandstone and gas diffusion layer for different wettabilities, as simulated by the Lattice Boltzmann Method. Red indicates gas and water is shown in blue for both rock and GDL domains. (For interpretation of the references to colour in this figure legend, the reader is referred to the web version of this article.)

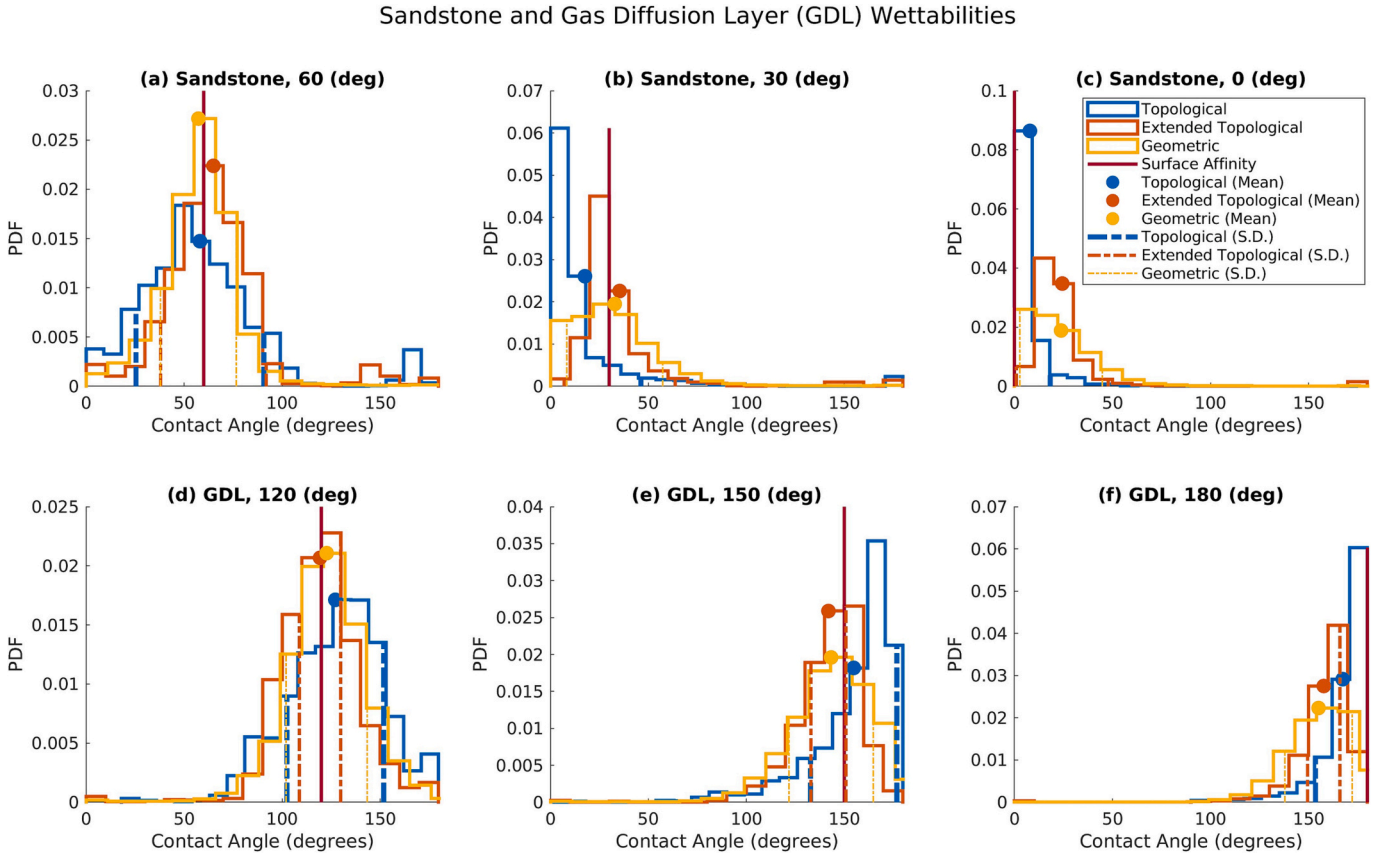


Fig. 9. Plots of the measured contact angles within the simulated domains in Fig. 8. (a-f) The original topological method shows the deviation in measurements consistent with previously shown deviations in simple clusters. The extended topological method and the geometric measurement method show good agreement with each other and the intrinsic contact angle set in the simulation. Geometric measurements show a wider variance due to contact loop variation, while topological methods show less accuracy and outliers in intermediate wetting conditions due to less accurate interface curvature measurements.

values on a per-voxel basis. This is visually depicted in Fig. 11a, showing zones of hydrophobic fiber and hydrophilic fiber emulating a GDL treated with PTFE. The case examined here is extreme, as it spans all possible contact angles, with relatively sharp transitions between wetting zones. This mixed-wetting domain is used as input for the same LBM simulation protocol as outlined in the previous Section 4.3, with the resulting steady state fluid distributions rendered in Fig. 11b. From this, the local contact angles of each cluster, for both phases – water

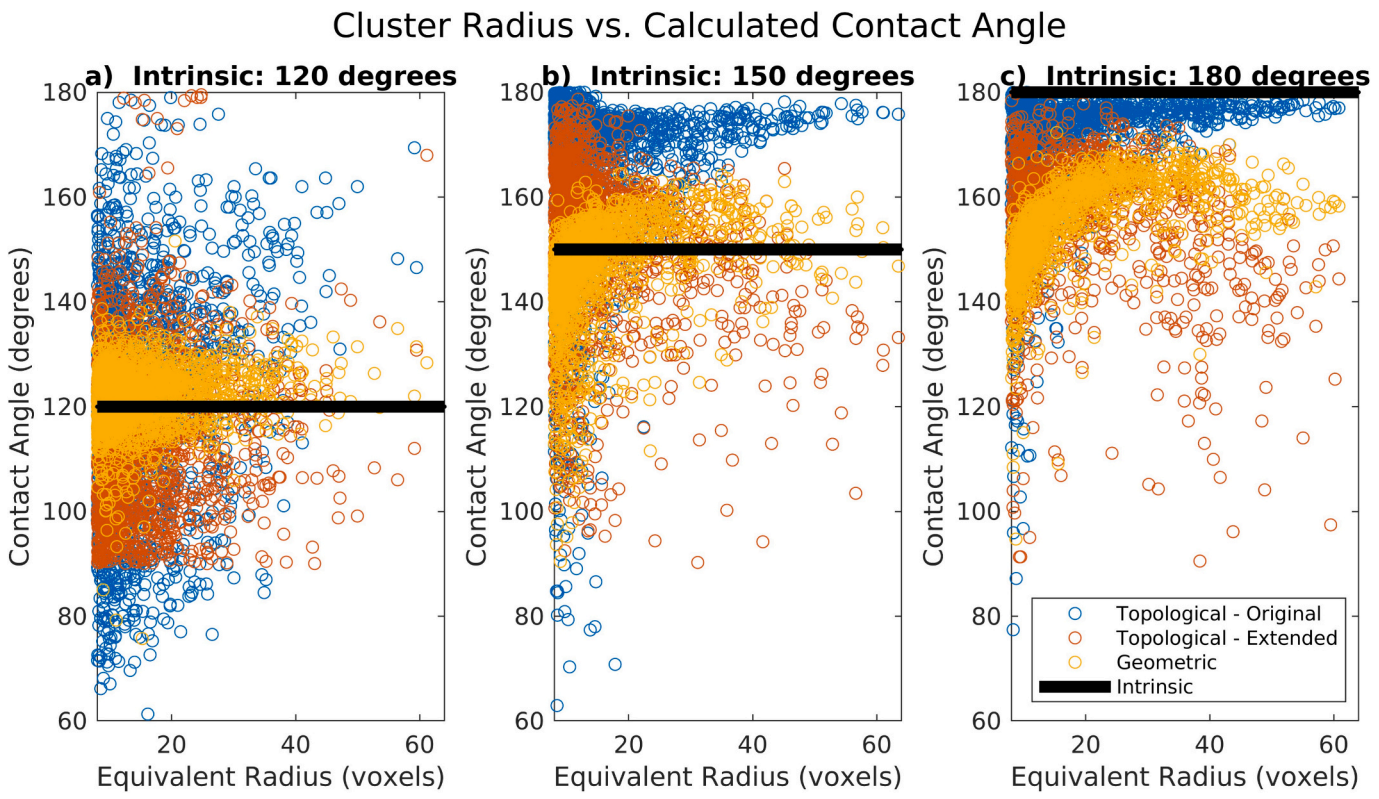


Fig. 10. The effect of smoothing and aliasing of ill-defined small clusters is seen as a deviation from intrinsic at small equivalent radii, and at the extreme of complete non-wetting, smoothing errors persist as underestimation due to deformation. Though these are plotted per cluster here, their small contact loop perimeters do not affect the overall mean wetting histograms but pose issues for the spatial accuracy of wettability maps of mixed wetting domains.

(phase 1) and gas (phase 2) are measured to obtain the contact angle map over the entire domain.

The contact angle at the contact loops of both phases is rendered in Fig. 11c-e for the geometric, topological, and extended topological methods. A coarse visual match can be seen over the sparse loop data for hydrophobic and hydrophilic regions, and data density is highest in regions of high clustering. This data density is governed by the volume fraction of each phase relative to the volume of the pore space that is non-wetting to said phase, also assuming the phase is present in the non-wetting region. Thus, in this case, the most data is collected for the water phase as it occupies a realistic and minor fraction of 30% of the volume and exists throughout the GDL. This is a typical spatial distribution and volume fraction of water found within the GDL during the operation of a PEMFC and represents the steady state condensation of water droplets from water vapor within a GDL [6]. In real experimental conditions of fluid invasion into mixed wetting media, it may be more difficult to establish the presence of a non-wetting phase in tight pore spaces due to capillary barriers. In these numerical experiments, a gradual condensation of one phase is simulated with spinodal decomposition, which for the case of the GDL, emulates water droplets condensing uniformly throughout the domain as the surrounding temperature slowly falls. This is achieved in the LBM simulation with initial and boundary conditions described in the previous Section 4.3. From this coarse visual match of measured contact angles on the contact loops, a full contact angle map and comparison over the domain can be obtained by natural neighbor interpolation [37] over the full domain.

The geometric, topological, and extended topological methods are used to obtain comparative contact angle maps, which can be seen in Fig. 12a-c. The interpolation of the contact angle over the full solid phase performs well for this test case due to the Gaussian distribution of wetting over the domain. All methods visually show an accurate overall characterization of water-wetting and gas-wetting regions. The error maps in Fig. 12d-f also show that local errors are limited to approximately 30^o in isolated outlier clusters. In regions of neutral wetting (near 90^o), topological methods also tend to over-estimate the contact angle. These spatially visible trends are confirmed by a plot of the measured contact angles from the simulated clusters against the assigned contact angles in the simulation in Fig. 12g-i.

The overall absolute error ($\frac{\sum|\theta_{measured}-\theta_{assigned}|}{N}$) over the entire domain is 9.1^o for geometric methods and 19.4^o and 14.0^o for the topological and extended topological methods respectively. In general, the error bands indicate that the geometric method gives the tightest and most accurate result, while extended topological methods improve the widely scattered results from the original topological method. The calculated standard deviation of the error supports this observation, with values of 11.4^o, 24.0^o, and 17.5^o for geometric, topological, and extended topological methods respectively. This is expected, as topological methods effectively operate at a length scale above the voxel resolution of the domain. The topological method calculates a single contact angle for each cluster, while the extended topological method calculates a single contact angle for each contact loop within each cluster. This measurement of singular values at the cluster scale naturally introduces spatial error and noise at the voxel scale. This is not an issue with geometric methods, as they individually calculate the contact angle at every voxel along every contact loop. In the case where a single contact loop is in contact with multiple contact angles, the geometric method will locally measure the contact angle at the location, thus the resulting values of contact angle measured at the contact loop nodes will reflect the local apparent contact angle of the fluid cluster. Based on the fluid and solid configuration, some smearing of the contact angle would occur at the boundary, resulting in a continuously changing apparent contact angle through this region. In the case of topological methods, the original topological method would return a single “cluster-averaged value” of the effective wettability that influences the shape of the cluster of interest. In the extended topological method, the influence of a varying

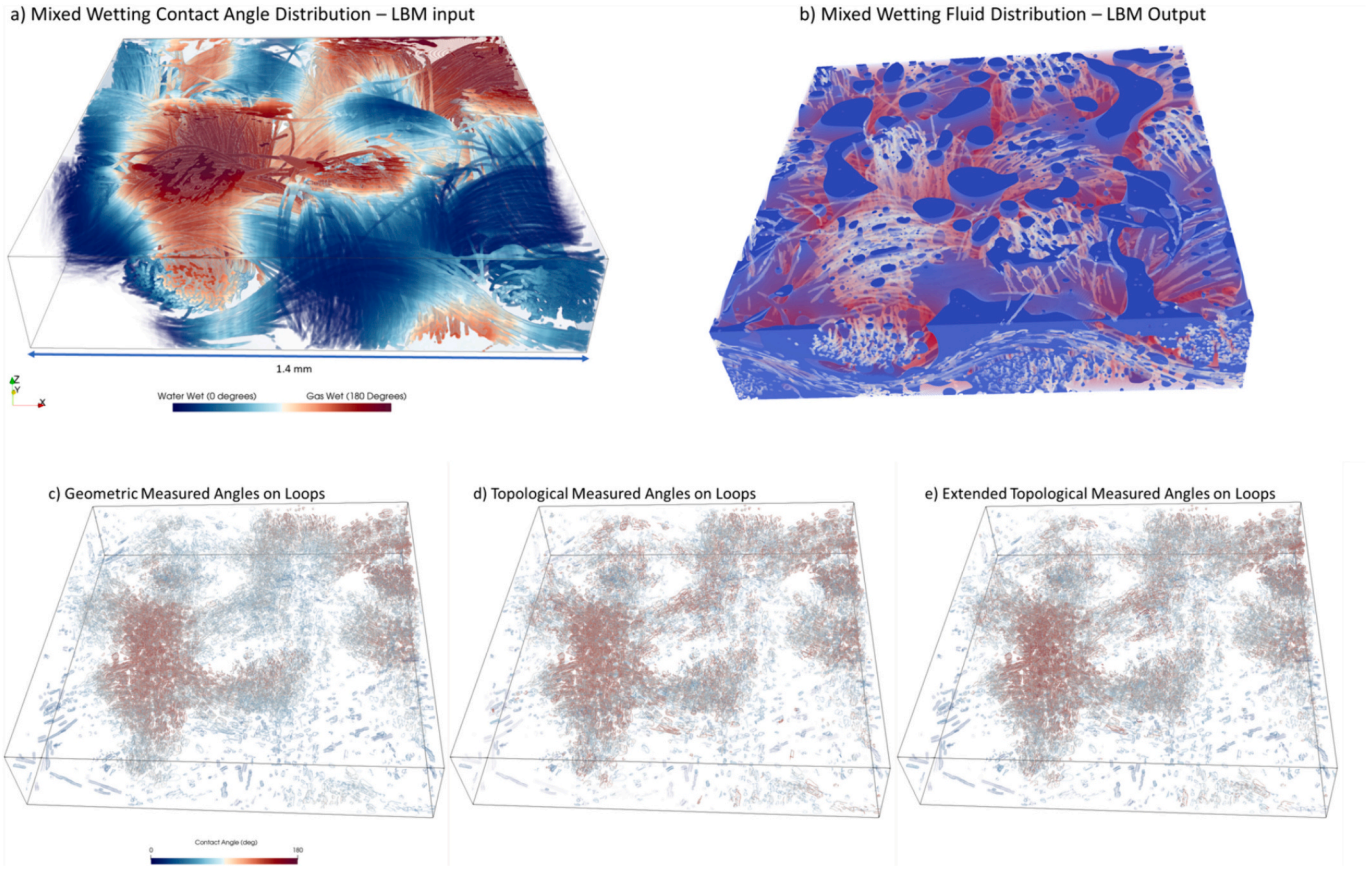


Fig. 11. 3D renders of a) the contact angle distribution assigned over the solid phase of the domain, spanning hydrophobic (gas wetting), neutral, and hydrophilic zones, and b) the resulting fluid distributions of water (blue) and gas (red) as simulated by LBM. The contact angle at the contact loops of both phases is rendered for c) geometric, d) topological, and e) extended topological methods, with a coarse visual match for hydrophobic and hydrophilic regions, and data density highest in regions of high clustering of the less abundant phase (30% water). (For interpretation of the references to colour in this figure legend, the reader is referred to the web version of this article.)

contact angle on a contact loop would manifest as variation in the measured value of ϕ, the product of the normal vector to the solid-fluid surface at the contact loop and the contact loop curvature. This is not directly the local measurement, as the sum of Gaussian curvature on the fluid-fluid interface also has an averaging effect on the calculation using the extended topological method.

At extreme contact angles ($<20^o$ and $>160^o$), all methods struggle to accurately measure the contact angle, since these surface wetting conditions generate vanishingly thin droplets that are intrinsically difficult to measure, even experimentally, as the mesh/voxels possess a finite volume. For geometric methods that only see the contact line and nearby fluid and solid surface meshes, this results in over-estimation at low contact angles and under-estimation at large contact angles. For topological methods, no specific bias in error exists at these extreme angles from curvature measurements. At neutrally wetting conditions (around 90^o), topological methods tend to overestimate the contact angle by up to 45^o for the original method, and 25^o for the extended method and in general become less accurate and more scattered. This is due to both the issue of cluster scale measurement *vs.* voxel scale measurement discussed in the previous paragraph, as well as errors in the measurement of the total Gaussian curvature $\sum \kappa_{G_i} A_i$. At intermediate contact angles, clusters tend to be more complex in shape and curvature. Saddle points and flatter regions become more common, which are difficult to smooth without significant deformation, even at the 5% shrinkage limit of this study. This issue is not as significant for contact loop smoothing as their loop curvature vectors are more independent of the contact angle which is measured on the solid and fluid surface meshes that are orthogonal to the loop. Thus for mixed wetting domains, the extended topological method significantly reduces the spread of measurements compared to the original topological method. The geometric method remains the most accurate due to i) the meshing algorithm outlined in Section 3.1.1 enforcing contact loop accuracy, ii) the issue of cluster-scale and voxel-scale resolution of measurements, and iii) complexities of surface curvatures at intermediate wetting conditions.

5. Conclusions

This study offers pivotal advancements in the understanding and assessment of *in situ* wettability in porous materials, which has critical implications for the performance and efficiency of CO_2/H_2 geo-storage, fuel cells, electrolyzers, filtration systems, and catalysts. The wettability distributions of these materials are often complex, subject to spatial variations and influenced by dynamic forces, chemical heterogeneity, and surface roughness. Current *in situ* measurements, while offering localized insights into wettability, face challenges in accurately capturing the nuances of multiphase fluid interactions in voxelized 3D domains.

A novel and transformative approach is introduced in this study with a specific focus on mixed wettability domains. An extended topological method for *in situ* contact angle measurement is presented, as well as a detailed and simplified implementation and analysis of the ill-posed meshing stage alongside geometric methods of measurement. These new methods and improved techniques surpass the accuracy and reliability of existing topological methods and perform comparably to geometric methods on uniformly wetting systems. The issues that topological methods have of effectively existing at one length scale above

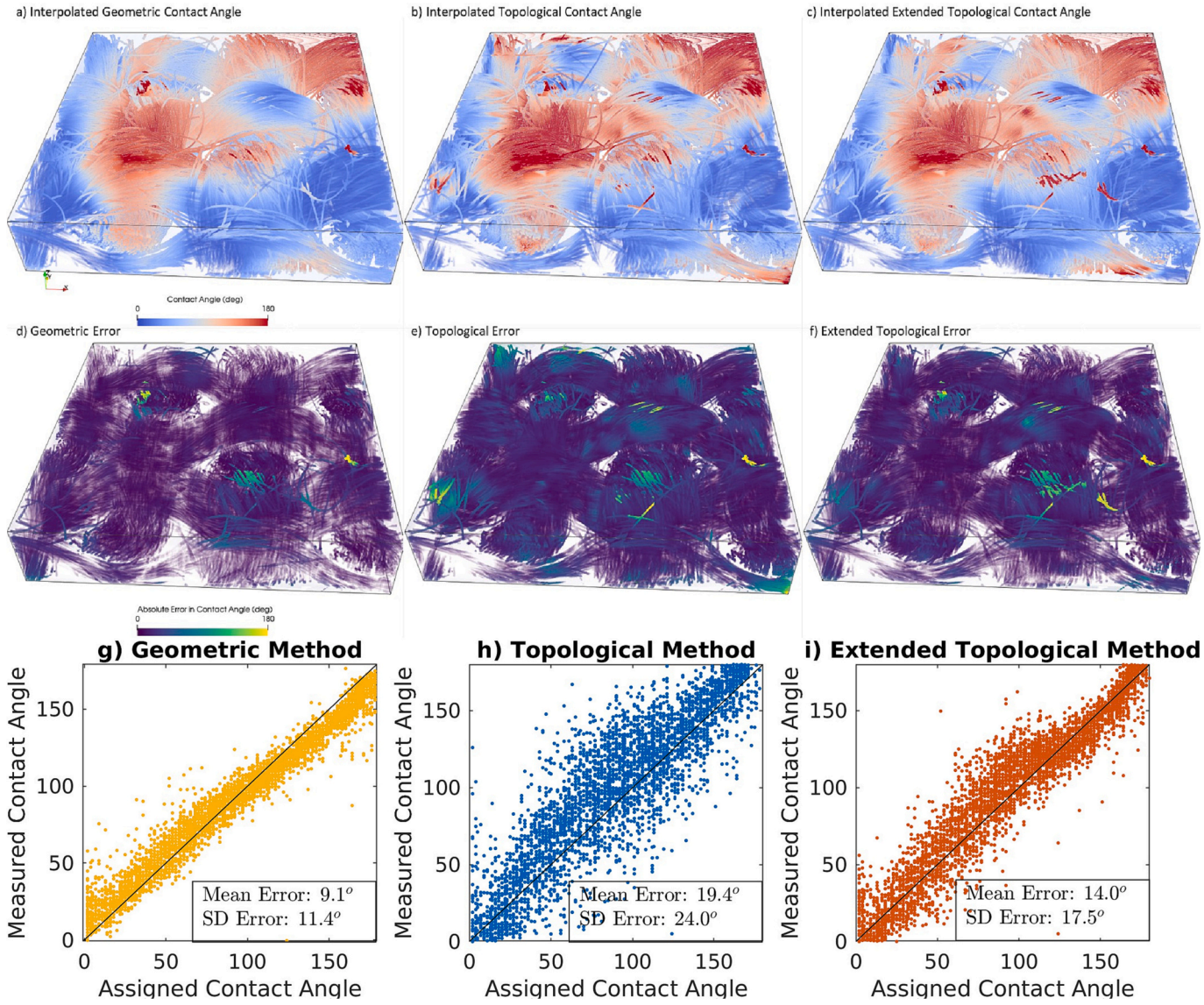


Fig. 12. Renders and plots of the measured and interpolated contact angle fields for the methods in this study. (a-c) Show the resulting interpolated contact angle field using natural neighbor interpolation from the loop data in Fig. 11c-e, and (d-f) show the local absolute error in measured contact angle. (g-i) Plot the interpolated contact angles against the original contact angle map assigned to the LBM simulations. Under/over estimation is seen at extreme angles with the geometric method due to mesh and voxel detail for vanishingly thin clusters. Increased error due to saddle curvatures and complex cluster geometries is seen at intermediate contact angles for topological methods. Overall, extended topological methods improve on the original method while geometric methods perform best for these mixed-wet cases.

the contact loop voxels – the cluster scale, as well as the sensitivity of Gaussian curvature measurements at intermediate wetting conditions are explored and compared with geometric methods, showing that geometric methods continue to excel in mixed-wetting domains aside from meshing biases at extreme contact angles, illustrating a nuanced interplay of these methodologies in assessing wettability for mixed-wet systems. Geometric methods in this study have been shown overall to perform on-par or even better than the topological and extended topological methods in terms of measurement accuracy, with similar computational cost. In certain instances of highly non-wetting/wetting systems, where fluid clusters do not contact the solid surface upon segmentation of the multiphase image, the original topological method works best as it does not require discrimination of the contact loop or the fluid-fluid and fluid-solid interfaces. In cases of difficult or poorly-resolved image segmentation, a combination of the extended topological method and geometric methods would provide sufficient information to improve the confidence of the calculated result.

Accompanying this research is a comprehensive open-source platform enabling the scientific community to delve deeper into *in situ* wettability characterization beyond its origins in geoscience.

In conclusion, we provide precise tools for measuring *in situ* wettability on porous structures, and ultimately, understanding and optimizing fluid and energy transfer in porous materials. The methods introduced in this study have the potential to dramatically enhance the performance of critical porous structure applications and signify a stride toward more efficient and sustainable systems.

CRediT authorship contribution statement

Ying Da Wang: Conceptualization, Formal analysis, Investigation, Methodology, Resources, Software, Validation, Visualization, Writing – original draft, Writing – review & editing. **Luke M. Kearney:** Conceptualization, Methodology, Writing – original draft. **Martin J. Blunt:** Conceptualization, Data curation, Methodology, Writing – original

draft, Writing – review & editing. **Chenhao Sun:** Conceptualization, Data curation, Methodology, Writing – review & editing. **Kunning Tang:** Data curation, Writing – original draft, Writing – review & editing. **Peyman Mostaghimi:** Data curation, Project administration, Resources, Supervision, Writing – review & editing. **Ryan T. Armstrong:** Conceptualization, Investigation, Methodology, Project administration, Supervision, Writing – review & editing.

Declaration of competing interest

The authors declare no conflicts of interest.

Data availability

Code is available at https://github.com/yingDaWang-UNSW/inSituContactAngles.

Acknowledgments

R. T. A. and P. M. acknowledges Australian Research Council Discovery (DP210102689). This research/project was undertaken with the assistance of resources and services from the National Computational Infrastructure (NCI), which is supported by the Australian Government.

Appendix A. Appendix

A.1. Extended topological method

Here, we generalise the relationship between Gaussian curvature and wettability derived by [22,23] and [25] to account for the orientation of the solid surface at the contact line. We follow the vectorial approach used in the supplementary material of [22].

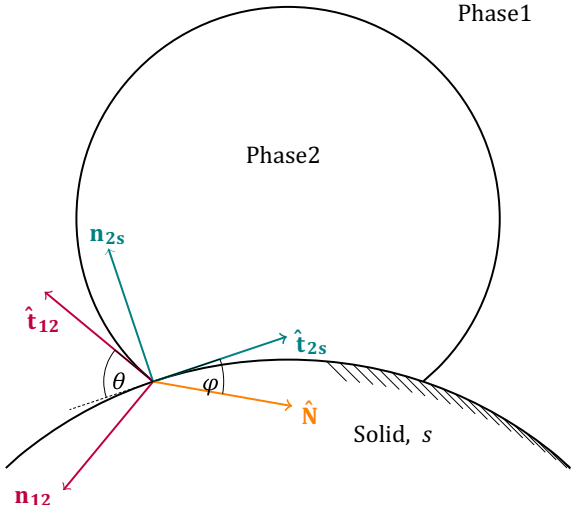


Fig. 13. Diagram of a sessile droplet depicting the relevant vectors and notations used in the following derivation, based on Fig. S1 from [22].

The Gauss-Bonnet theorem relates the geometry of an object to its topology [38],

$$\int_M KdA + \int_{\partial M} k_g ds = 2\pi\chi(M), \tag{3}$$

where K is the total Gaussian curvature, dA is an infinitesimal area element on the surface M of the object, k_g is the geodesic curvature, ds is an infinitesimal arc length element along the contact line ∂M and $\chi(M)$ is the Euler characteristic of the surface. The Euler characteristic is a topological invariant of any manifold (object, surface, *etc.*) and for this application can be expressed in terms of three Betti numbers,

$$\chi = N - L + O, \tag{4}$$

where informally N is the number of disconnected objects, L is the number of loops and O is the number of cavities. We deviate from previous derivations [22,23,25] by applying the Gauss-Bonnet theorem to the fluid-fluid interface (*i.e.*, the meniscus) M_{12}, instead of the entire object, giving

$$\int_{M_{12}} KdA + \int_{\partial M} k_{g12} ds = 2\pi\chi(M_{12}), \tag{5}$$

where k_{g12} is the geodesic curvature of the meniscus. The geodesic curvature of the meniscus is the magnitude of the curvature vector $\mathbf{k}$ projected onto the meniscus, thus

$$k_{g12} = \boldsymbol{k} \bullet \hat{\boldsymbol{t}}_{12}, \tag{6}$$

where $\hat{\boldsymbol{t}}_{12}$ is the unit tangent vector of the meniscus. The curvature vector is oriented in the direction normal to the contact line $\hat{\boldsymbol{N}}$,

$$k_{g12} = k(\hat{\boldsymbol{N}} \bullet \hat{\boldsymbol{t}}_{12}), \tag{7}$$

where $k = ||\mathbf{k}||$ is the magnitude of the curvature of the contact line. The angle between these two vectors is $(\pi - \theta + \phi)$, where θ is the contact angle and ϕ is the angle measured anticlockwise from $\widehat{N}$ to $\widehat{t}_{2s}$ (Fig. 13). The angle ϕ thus quantifies the relative orientation of the solid to the plane containing the contact line. Therefore,

$$k_{g12} = -k\,cos(\theta - \phi). \tag{8}$$

The second term of Eq. (5), often referred to as the deficit curvature $k_d(M_{12})$, is the integral of this geodesic curvature along the contact line. Assuming that the contact line lies within a plane, the total curvature $\int_{\partial M} k\,ds = 2\pi$. Since k is the reciprocal of the radius of curvature, a change of variables can be performed, $k\,ds = du$, where u is an angular coordinate along the contact line, giving

$$k_d(M_{12}) = -\int_0^{2\pi} cos(\theta - \phi)du. \tag{9}$$

The Gauss-Bonnet theorem relates the deficit curvature to the Gaussian curvature and the Euler characteristic of an object. An object with n menisci and N_{loops} contact line loops in total has an Euler characteristic $\chi(M_{12}) = 2n - N$. For example, a meniscus with no contact lines is homologous to a sphere, or a meniscus with two contact lines is homologous to a disk with two holes. Substituting the expression for the Euler characteristic and Eq. (9) into Eq. (5) yields

$$2\pi N - \sum_{i=0}^{N}\int_0^{2\pi} cos(\theta - \phi)du_i = 4\pi n - \int_{M_{12}} KdA, \tag{10}$$

where we have summed the deficit curvatures of each contact line. We simplify this expression by assuming that θ and ϕ are constant along each contact line, to arrive at

$$2\pi N(1 - cos(\theta - \phi)) = 4\pi n - \int_{M_{12}} \mathrm{K}dA, \tag{11}$$

Rearranging for contact angle gives

$$\theta = \phi + cos^{-1}\left(1 - \frac{4\pi n - \int_{M_{12}} KdA}{2\pi N_{loops}}\right). \tag{12}$$

The orientation angle ϕ is defined as

$$\phi = cos^{-1}(\widehat{N} \bullet \widehat{n}_{2s}) - \frac{\pi}{2}, \tag{13}$$

where $\widehat{n}_{2s}$ is the unit normal vector to the solid at the contact line.

A.2. Supplementary Figure 1

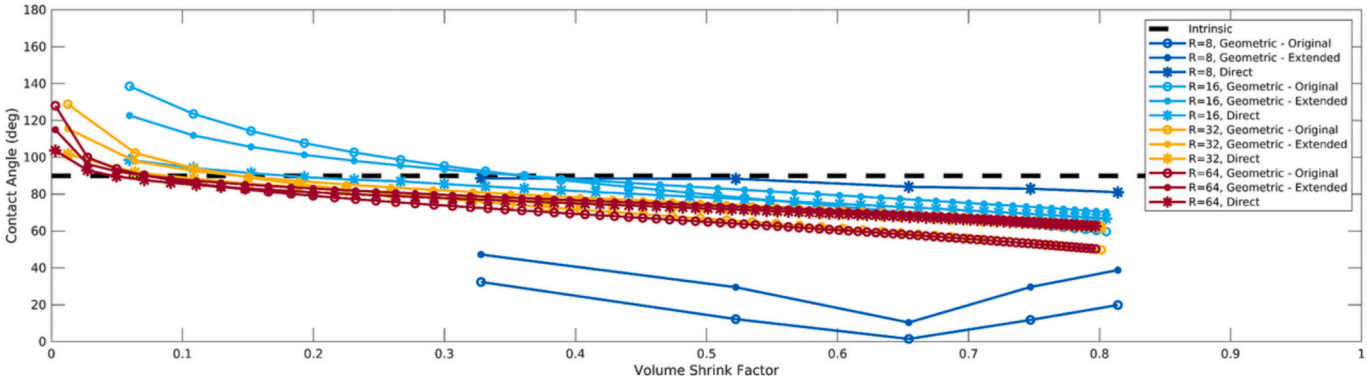


Fig. 14. Calculated contact angle of voxelized fluid clusters of hemispheres at diameters of 8, 16, 32, and 64 voxels as a function of the calculation method and the degree of smoothing (shrinkage). The idea of an "intrinsic contact angle" breaks down around $D < 16$ due to aliasing, and smoothing results in a reasonable calculated value of the contact angle at <10% shrinkage. The geometric method performs most consistently as it does not require surface curvatures, and the smoothing algorithm in this study preserves contact loop sharpness which is flat in the z-direction.

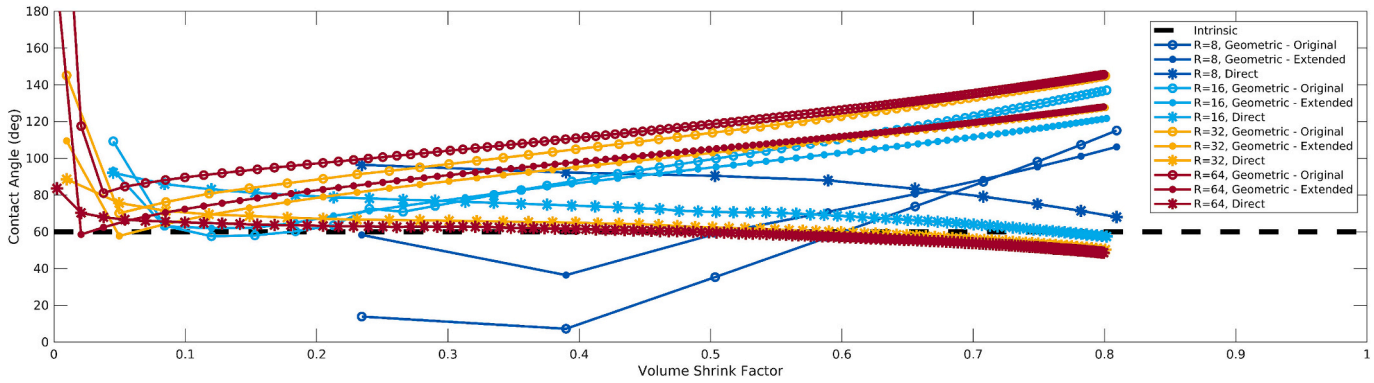


Fig. 15. Calculated contact angle of voxelized fluid clusters of spheres on curved surfaces at diameters of 8, 16, 32, and 64 voxels as a function of the calculation method and the degree of smoothing (shrinkage). In this case, the geometric method and the extended topological methods perform most accurately since the smoothing of surfaces plays a larger role and the contact loop is affected by aliasing in 3 orientations. The original topological method shows its characteristic acute/obtuse angle deviation.

References

[1] Arif M, Abu-Khamsin SA, Iglauer S. Wettability of rock/co2/brine and rock/oil/co2-enrichedbrine systems: critical parametric analysis and future outlook. Adv Colloid Interface Sci 2019;268:91–113.

[2] Pan B, Ni T, Zhu W, Yang Y, Ju Y, Zhang L, et al. Mini review on wettability in the methane–liquid–rock system at reservoir conditions: implications for gas recovery and geo-storage. Energy Fuel 2022;36(8):4268–75.

[3] Higgs S, Da Wang Y, Sun C, Ennis-King J, Jackson SJ, Armstrong RT, et al. In-situ hydrogen wettability characterisation for underground hydrogen storage. Int J Hydrogen Energy 2022;47(26):13062–75.

[4] Higgs S, Da Wang Y, Ennis-King J, Jackson S, Sun C, Armstrong R, et al. Direct measurement of hydrogen relative permeability hysteresis for underground hydrogen storage. Available at SSRN 4310400. 2022.

[5] Wang Y, Liu T, He W, Wang S, Liu S, Yue L, et al. Performance enhancement of polymer electrolyte membrane fuel cells with a hybrid wettability gas diffusion layer. Energ Conver Manage 2020;223:113297.

[6] Wang YD, Meyer Q, Tang K, McClure JE, White RT, Kelly ST, et al. Large-scale physically accurate modelling of real proton exchange membrane fuel cell with deep learning. Nat Commun 2023;14(1):745.

[7] Shojaei MJ, Bijeljic B, Zhang Y, Blunt MJ. Minimal surfaces in porous materials: X-ray image-based measurement of the contact angle and curvature in gas diffusion layers to design optimal performance of fuel cells. ACS Appl Energy Mater 2022;5(4):4613–21.

[8] Wang Y, Liu T, He W, Wang S, Liu S, Yue L, et al. Performance enhancement of polymer electrolyte membrane fuel cells with a hybrid wettability gas diffusion layer. Energ Conver Manage 2020;223:113297.

[9] Anderson W. Wettability literature survey-part 2: wettability measurement. J Petrol Tech 1986;38(11):1246–62.

[10] Pan B, Yin X, Iglauer S. A review on clay wettability: from experimental investigations to molecular dynamics simulations. Adv Colloid Interface Sci 2020;285:102266.

[11] Boinovich L, Emelyanenko A. The prediction of wettability of curved surfaces on the basis of the isotherms of the disjoining pressure. Colloids Surf A Physicochem Eng Asp 2011;383(1–3):10–6.

[12] Sobczak N, Singh M, Asthana R. High-temperature wettability measurements in metal/ceramic systems–some methodological issues. Curr Opin Solid State Mater Sci 2005;9(4–5):241–53.

[13] Eustathopoulos N, Sobczak N, Passerone A, Nogi K. Measurement of contact angle and work of adhesion at high temperature. J Mater Sci 2005;40:2271–80.

[14] Al-Yaseri A, Wolff-Boenisch D, Fauziah CA, Iglauer S. Hydrogen wettability of clays: implications for underground hydrogen storage. Int J Hydrogen Energy 2021;46(69):34356–61.

[15] Wan J, Kim Y, Tokunaga TK. Contact angle measurement ambiguity in supercritical co2–water–mineral systems: mica as an example. Int J Greenh Gas Control 2014;31:128–37.

[16] Andrew M, Bijeljic B, Blunt MJ. Pore-scale contact angle measurements at reservoir conditions using x-ray microtomography. Adv Water Resour 2014;68:24–31.

[17] Khishvand M, Alizadeh A, Oraki Kohshour I, Piri M, Prasad R. In situ characterization of wettability alteration and displacement mechanisms governing recovery enhancement due to low-salinity waterflooding. Water Resour Res 2017;53(5):4427–43.

[18] Scanziani A, Singh K, Blunt MJ, Guadagnini A. Automatic method for estimation of in situ effective contact angle from x-ray micro tomography images of two-phase flow in porous media. J Colloid Interface Sci 2017;496:51–9.

[19] Rabbani A, Sun C, Babaei M, Niasar VJ, Armstrong RT, Mostaghimi P. Deepangle: fast calculation of contact angles in tomography images using deep learning. Geoenergy Sci Eng 2023;227:211807.

[20] Wang YD, Blunt MJ, Armstrong RT, Mostaghimi P. Deep learning in pore scale imaging and modeling. Earth-Sci Rev 2021;215:103555.

[21] AlRatrout A, Raeini AQ, Bijeljic B, Blunt MJ. Automatic measurement of contact angle in pore-space images. Adv Water Resour 2017;109:158–69.

[22] Sun C, McClure JE, Mostaghimi P, Herring AL, Berg S, Armstrong RT. Probing effective wetting in subsurface systems. Geophys Res Lett 2020;47(5). pp. no–no.

[23] Sun C, McClure JE, Mostaghimi P, Herring AL, Meisenheimer DE, Wildenschild D, et al. Characterization of wetting using topological principles. J Colloid Interface Sci 2020;578:106–15.

[24] Sun C, McClure JE, Mostaghimi P, Herring AL, Shabaninejad M, Berg S, et al. Linking continuum-scale state of wetting to pore-scale contact angles in porous media. J Colloid Interface Sci 2020;561:173–80.

[25] Blunt MJ, Akai T, Bijeljic B. Evaluation of methods using topology and integral geometry to assess wettability. J Colloid Interface Sci 2020;576:99–108.

[26] Wang YD, Armstrong RT, Mostaghimi P. Boosting resolution and recovering texture of 2d and 3d micro-ct images with deep learning. Water Resour Res 2020;56(1). https://doi.org/10.1029/2019WR026052. p. e2019WR026052.

[27] Wang YD, Armstrong RT, Mostaghimi P. Enhancing resolution of digital rock images with super resolution convolutional neural networks. J Petrol Sci Eng 2019;182:106261.

[28] Tang K, Meyer Q, White R, Armstrong RT, Mostaghimi P, Da Wang Y, et al. Deep learning for full-feature x-ray microcomputed tomography segmentation of proton electron membrane fuel cells. Computers & Chemical Engineering 2022;161:107768.

[29] Wang YD, Shabaninejad M, Armstrong RT, Mostaghimi P. Deep neural networks for improving physical accuracy of 2d and 3d multi-mineral segmentation of rock micro-ct images. Appl Soft Comput 2021;104:107185.

[30] Wang YD, Chung T, Rabbani A, Armstrong RT, Mostaghimi P. Fast direct flow simulation in porous media by coupling with pore network and Laplace models. Adv Water Resour 2021;150:103883.

[31] McClure JE, Li Z, Berrill M, Ramstad T. The LBPM software package for simulating multiphase flow on digital images of porous rocks. Comput Geosci 2021:1–25.

[32] Wang Y, Chung T, Armstrong R, McClure J, Ramstad T, Mostaghimi P. Accelerated computation of relative permeability by coupled morphological and direct multiphase flow simulation. J Comput Phys 2020;401:108966.

[33] Lorensen WE, Cline HE. Marching cubes: a high resolution 3d surface construction algorithm. SIGGRAPH Comput Graph Aug 1987;21:163–9.

[34] Nealen A, Igarashi T, Sorkine O, Alexa M. Laplacian mesh optimization. In: Proceedings of the 4th international conference on Computer graphics and interactive techniques in Australasia and Southeast Asia; 2006. p. 381–9.

[35] Sun C, McClure JE, Mostaghimi P, Herring AL, Berg S, Armstrong RT. Probing effective wetting in subsurface systems. Geophys Res Lett 2020;47(5). https://doi.org/10.1029/2019GL086151. p. e2019GL086151.

[36] Legland D, Kiêu K, Devaux M-F. Computation of minkowski measures on 2d and 3d binary images. Image Anal Stereol May 2011;26:83–92.

[37] Sibson R. A brief description of natural neighbour interpolation. Interpret Multivar Data 1981:21–36.

[38] Allendoerfer CB, Weil A. The Gauss-Bonnet theorem for Riemannian polyhedra. Trans Am Math Soc 1943;53(1):101–29.